PCCP

ROYAL SOCIETY OF CHEMISTRY

PAPER

View Article Online
View Journal | View Issue

Check for updates

Cite this: *Phys. Chem. Chem. Phys.*, 2025, **27**, 18927

Surface state activation driving charge separation *via* Z-scheme Fe_2O_3/CuO heterojunctions for photocatalytic H_2 evolution

Ke Ma, Jingying Wei, Chun Gou, Huaiguo Xue, Jingqi Tian and Tengfei Jiang *

Surface state modulation has emerged as a promising strategy to reduce rapid carrier recombination in photocatalytic reactions. However, surface states can paradoxically serve as indirect recombination centers due to sluggish interfacial reaction kinetics. Herein, the charge separation function of Ni-mediated surface states is reactivated *via* Z-scheme charge transfer engineering in Fe_2O_3/CuO heterojunctions, where the surface states spontaneously accumulate photoinduced electrons for efficient photocatalytic hydrogen production. Density functional theory (DFT) calculations reveal that Ni heteroatoms introduce surface states proximal to the conduction band minimum of CuO, creating electron-trapping configurations that facilitate the accumulation of photogenerated electrons. Surface photovoltage spectra demonstrate that Ni-induced surface states function as electron trapping centers, creating electron reservoirs that spatially decouple reduction sites from recombination sites. Time-resolved surface photovoltage decay kinetics quantitatively resolve the electron capture process occurring in the sub millisecond time scale, with carrier lifetimes prolonged to 4.72 ms with a 5-fold enhancement. This interfacial electron reservoir effect enhances the photocatalytic H_2 evolution rate of 1933.69 μmol g^{-1} h^{-1}, while maintaining 98% activity over 4 cycles. This work not only elucidates the mechanism of transition metal dopants in regulating surface states but also provides a new paradigm for designing photocatalytic interfaces with dynamic electron accumulation capabilities.

Received 11th July 2025,
Accepted 13th August 2025

DOI: 10.1039/d5cp02648b

rsc.li/pccp

Published on 01 septembrie 2025. Downloaded on 02.02.2026 22:20:06.

Introduction

As a crucial pathway for solar energy conversion, the core challenge in photocatalysis lies in achieving efficient separation of photogenerated charge carriers.[1,2] Researchers have developed multidimensional strategies to optimize charge dynamics: heterojunction engineering establishes interfacial electric field-driven charge separation through band offset alignment;[3,4] defect state modulation introduces intermediate bandgap states *via* oxygen vacancies or dopants to trap charge carriers;[5–8] and noble metal cocatalysts facilitate electron enrichment through Schottky barrier effects.[9–12]

Surface states function as pivotal interfacial charge-exchange platforms in photocatalytic systems,[13,14] where their energy levels, density-of-state distributions, and temporal evolution characteristics govern the transport pathways and ultimate fate of photogenerated carriers.[15] Thermodynamically, surface states act as "relay stations" for electron–hole pairs, modulating the competition between carrier recombination and migration through selective trapping/release mechanisms.[16,17] Kinetically, these states regulate interfacial charge transfer rates *via* non-adiabatic coupling effects.[18,19] Conventional surface-state engineering approaches typically employ defect-introduction strategies (*e.g.*, controlled oxygen vacancy generation) or exogenous molecular functionalization (*e.g.*, thiol ligand anchoring),[20] primarily focusing on creating deep-level localized surface states as charge reservoirs.[21] However, the surface states can paradoxically serve as indirect recombination centers due to sluggish interfacial reaction kinetics.[22,23] Therefore, an effective strategy is needed to overcome this limitation and enhance the efficiency of photocatalysis. Z-scheme charge transfer engineering in Fe_2O_3/CuO heterojunctions effectively modulates the charge transfer process,[24–26] thus enabling activation of surface states. Fe_2O_3 is an n-type semiconductor with a bandgap of approximately 2.0–2.2 eV. Its conduction band (CB) is located at about +0.3 V *vs.* NHE, while the valence band (VB) lies at approximately +2.3 V, endowing it with good visible-light responsiveness. CuO is a p-type semiconductor with a bandgap of about 1.2–1.7 eV, its CB and VB are positioned at roughly −0.3 V and +1.0 V, respectively. The staggered alignment of their CB and VB edges satisfies the energetic requirements for a Z-scheme heterojunction: electrons in the CB of Fe_2O_3 can recombine with holes in the VB of CuO,

School of Chemistry and Chemical Engineering, Yangzhou University, 180 Siwangting Road, Yangzhou 225002, People's Republic of China. E-mail: jiangtengfei@yzu.edu.cn

Published on 01 septembrie 2025. Downloaded on 02.02.2026 22:20:06.

thereby preserving the strong oxidation capability of Fe_2O_3 and the strong reduction capability of CuO.

In this paper, the charge separation function of Ni-mediated surface states is reactivated *via* Z-scheme charge transfer engineering in Fe_2O_3/CuO heterojunctions, where the surface states spontaneously accumulate photoinduced electrons for efficient photocatalytic hydrogen production. Density functional theory (DFT) calculations reveal that Ni heteroatoms introduce surface states proximal to the conduction band minimum of CuO, creating electron-trapping configurations that facilitate the accumulation of photogenerated electrons. Surface photovoltage spectra demonstrate that Ni-induced surface states function as electron trapping centers, creating electron reservoirs that spatially decouple reduction sites from recombination sites. Time-resolved surface photovoltage decay kinetics quantitatively resolve the electron capture process occurring in the sub millisecond time scale, with carrier lifetimes prolonged to 4.72 ms with a 5-fold enhancement. This interfacial electron reservoir effect enhances the photocatalytic H_2 evolution rate to 1933.69 μmol g^{-1} h^{-1}, while maintaining 98% of its initial activity over 4 cycles.

Materials and methods

All the chemicals used in this study were of analytical grade and used without further purification. Iron(III) nitrate nonahydrate ($Fe(NO_3)_3{\cdot}9H_2O$), copper(II) chloride dihydrate ($CuCl_2{\cdot}2H_2O$), nickel(II) sulfate hexahydrate ($NiSO_4{\cdot}6H_2O$), citric acid ($C_6H_8O_7$), and urea (CH_4N_2O) were purchased from Sigma-Aldrich Pte. Ltd. The water used throughout all experiments was purified using a Millipore system.

Materials preparation

Fe_2O_3/CuO heterojunctions were synthesized *via* a sol–gel combustion method using citric acid as the chelating agent. Specifically, 5 mmol $CuCl_2{\cdot}2H_2O$, 10 mmol $Fe(NO_3)_3{\cdot}9H_2O$, and $NiSO_4{\cdot}6H_2O$ (1%, 2%, and 4% molar ratio to iron) were dissolved in deionized water under magnetic stirring, forming precursor solution. Then 15 mmol anhydrous citric acid was added to the above solution, followed by magnetic stirring until complete dissolution, and 7.5 mmol urea was subsequently introduced into the mixture. The mixture was heated at 70 °C under continuous stirring until transitioning into a viscous gel. The gel underwent spontaneous combustion on a 170 °C hotplate, accompanied by vigorous gas evolution, ultimately yielding a dendritic black powder. After cooling, the combustion product was ground and calcined in a muffle furnace at 500 °C for 3 h. The resultant powders were subjected to three cycles of deionized water washing and drying. The final products were labeled as CFO500 (undoped), CFO500-1%Ni, CFO500-2%Ni, and CFO500-4%Ni.

Materials characterization

The surface morphology and elemental composition of the materials were analyzed using scanning electron microscopy (SEM, Zeiss Supra 55) coupled with energy-dispersive X-ray spectroscopy (EDX). High-resolution transmission electron microscopy (HRTEM) imaging and selected area electron diffraction patterns were acquired using a Tecnai G2 F30 S-TWIN transmission electron microscope operated at 200 kV. Crystal structure characterization was performed by X-ray diffraction (XRD) with 2θ ranging from 10° to 80° at a scanning rate of 2° min^{-1}. Optical properties were examined through UV-vis-NIR spectroscopy spanning 200–2000 nm in wavelength. For surface chemical analysis, X-ray photoelectron spectroscopy (XPS) measurements were conducted on 5 × 5 mm pelletized samples using monochromated Al K-α radiation (1486.6 eV), with charge compensation achieved by a neutralization gun. XPS spectra were collected in wide-scan (150 eV, 1 eV step) and narrow-scan (30 eV, 0.05 eV step) modes, with binding energy calibration referenced to the C 1s peak at 284.8 eV.

Photoelectrochemical and photocatalytic characterization

Photoelectrochemical measurements were conducted using an Autolab workstation with a 500 W xenon lamp (100 mW cm^{-2}). Working electrodes were fabricated by drop-coating 8 mg photocatalyst dispersed in 3 mL ethylene glycol methyl ether (30-min sonication) onto fluorine-doped tin oxide (FTO, 1 × 3 cm^2), followed by drying at 90 °C and calcination under N_2 at 200 °C for 30 min (3 °C min^{-1} ramp). Tests were performed in a 0.5 M Na_2SO_4 electrolyte with Pt counter and Ag/AgCl reference electrodes. Photocatalytic hydrogen evolution was evaluated by dispersing a 10 mg catalyst in 9 mL H_2O with 1 mL methanol (N_2-purged for 5 min), irradiated by a 500 W xenon lamp under continuous stirring for 4 h. Evolved H_2 was quantified *via* GC-2014 gas chromatography (TCD detector, N_2 carrier gas).

Surface photovoltage spectroscopy (SPS)

SPS utilized a lock-in amplifier-based system comprising a CHF-XM500 xenon lamp, SBP500 monochromator (23 Hz modulation), SR830 lock-in amplifier (10 MΩ input impedance), SR540 chopper, and sample cell. Wavelength scanning proceeded from long to short wavelengths, with a UV cut-off filter (λ > 420 nm) applied for measurements >600 nm. System calibration employed a Zolix DSI200 silicon detector to eliminate phase artifacts.

Results and discussion

The morphology and microstructure of the catalyst were analyzed using scanning electron microscopy (SEM) and transmission electron microscopy (TEM). As shown in Fig. 1a and b, the SEM images reveal that CFO500 consists of amorphous nanoparticles with rough surfaces. After nickel doping, no significant morphological changes were observed. The presence of Cu, Fe, and O elements, as well as Fe_2O_3 and CuO, was further confirmed by the elemental distribution maps in Fig. 1c–g. In the high-resolution transmission electron microscopy (HRTEM) images (Fig. 1h and i), the HRTEM image of the Fe_2O_3/CuO heterojunction shows the interface between Fe_2O_3 and CuO. The

 This journal is © the Owner Societies 2025

Published on 01 septembrie 2025. Downloaded on 02.02.2026 22:20:06.

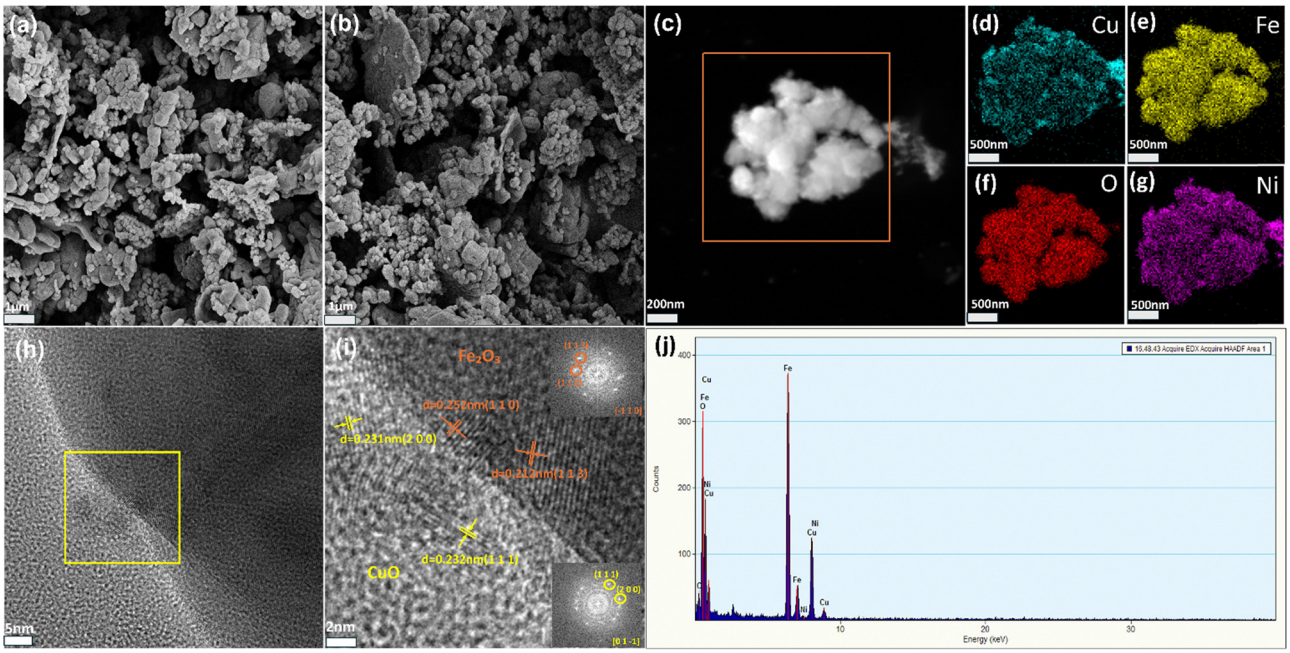

Fig. 1 (a) and (b) SEM images of CFO500 and CFO500-2%Ni. (c)–(g) Elemental distribution mapping images of CFO500-2%Ni. (h) and (i) HRTEM electron microscopy image of CFO500-2%Ni. (j) EDS spectrum of CFO500-2%Ni.

lattice spacings of 0.252 nm and 0.212 nm correspond to the (110) and (113) crystallographic planes of Fe_2O_3 (JCPDS 33-0664), with the crystallographic zone axis of Fe_2O_3 being [–110]. The lattice spacings of 0.231 nm and 0.232 nm correspond to the

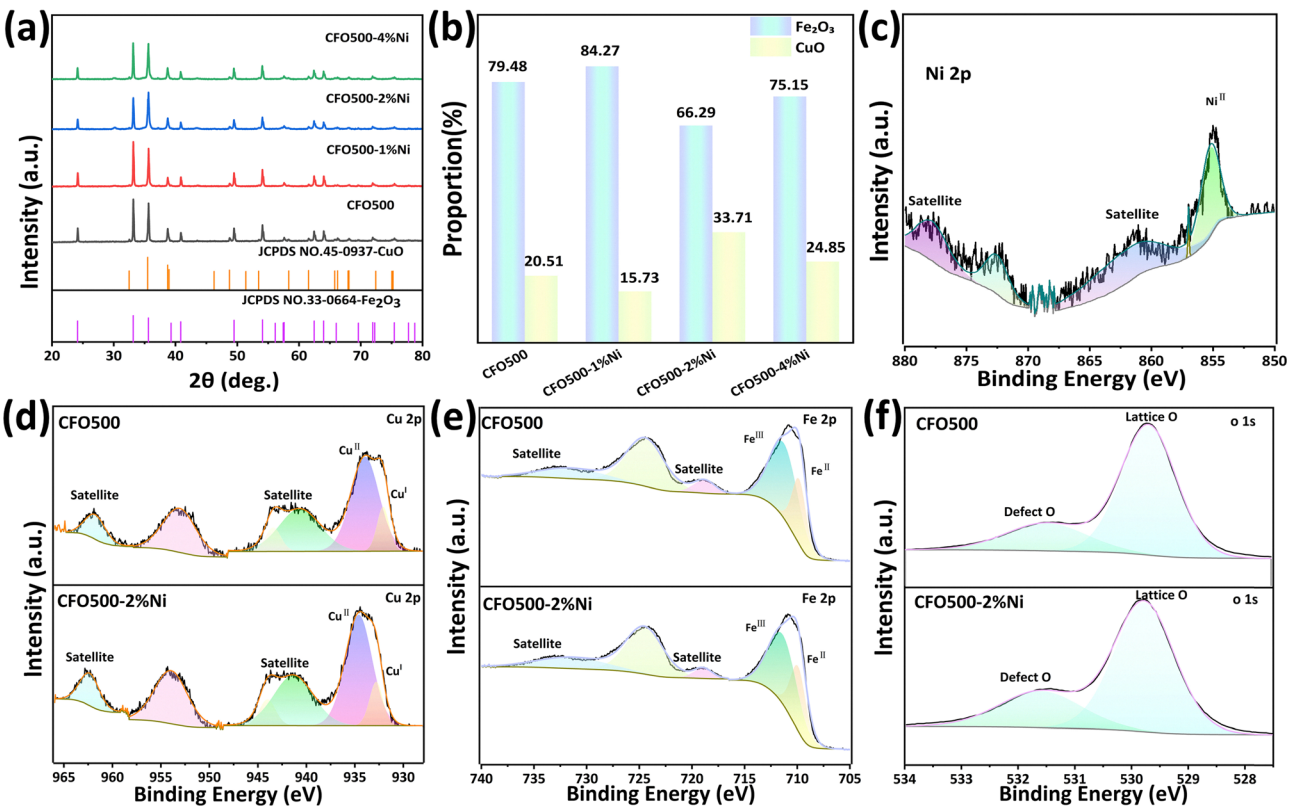

Fig. 2 (a) XRD patterns of CFO500, CFO500-1%Ni, CFO500-2%Ni and CFO500-4%Ni; (b) refined phase composition of CFO; (c) Ni 2p spectrum of CFO500-2%Ni; (d) Cu 2p spectra of CFO500 and CFO500-2%Ni; (e) Fe 2p spectra of CFO500 and CFO500-2%Ni; (f) O 1s spectra of CFO500 and CFO500-2%Ni.

Published on 01 septembrie 2025. Downloaded on 02.02.2026 22:20:06.

(200) and (111) crystallographic planes of CuO (JCPDS 65-2309), with the crystallographic zone axis of CuO being [01–1]. The composition of the Fe_2O_3/CuO heterojunction was confirmed by energy dispersive spectroscopy (EDS) in Fig. 1j. The elemental distribution and HRTEM image of CFO500 are shown in Fig. S1.

The crystal structure of the CFO catalyst was characterized by powder X-ray diffraction (XRD). The XRD pattern of CFO is shown in Fig. 2a. The diffraction peaks at 24.1°, 33.1°, 35.6°, 40.8°, 49.4°, 54.0°, 62.4° and 63.9° correspond to the (012), (104), (110), (113), (024), (116), (214) and (300) crystal planes of Fe_2O_3 (JCPDS 33-0664), respectively. The diffraction peaks at 35.5°, 38.7°and 38.9° correspond to the (002), (111) and (200) crystal planes of CuO (JCPDS 65-2309), respectively. These results confirm the successful synthesis of CFO. To further investigate this, structural refinements were performed on four CFO samples with different nickel doping levels (CFO500, CFO500-1%Ni, CFO500-2%Ni, and CFO500-4%Ni). The Rietveld refinement results are shown in Fig. S2 and Table S1. The absence of NiO peaks (Fig. 2a) indicates that Ni^{2+} has been incorporated into the lattices of Fe_2O_3 and CuO. The content of Fe_2O_3 fluctuates between 66.29% and 84.27% due to nickel doping. The changes in the contents of Fe_2O_3 and CuO with nickel doping are shown in Fig. 2b.

XPS characterization was performed on CFO500 and CFO500-2%Ni samples to investigate the chemical states and compositions of surface elements. All binding energies were calibrated against the C 1s peak at 284.8 eV. The XPS spectra of CFO materials (Fig. 2c–f and Fig. S3e) reveal all elements associated with both CFO500 and CFO500-2%Ni. In Fig. 2c, the Ni 2p spectrum of CFO500-2%Ni exhibits a main Ni^{2+} peak at 855.23 eV (Ni $2p_{3/2}$) with a satellite peak at 861.99 eV. The Ni $2p_{1/2}$ region displays a main peak at 872.53 eV and a satellite peak at 877.78 eV. As shown in Fig. 2d, for CFO500, the Cu $2p_{1/2}$ region exhibits a main peak at 953.08 eV and a satellite peak at 961.77 eV, while the Cu $2p_{3/2}$ region shows a main peak at 933.95 eV (corresponding to Cu^{2+}) with satellite peaks at 943.42 eV and 940.69 eV. For CFO500-2%Ni, the Cu $2p_{1/2}$ peaks are observed at 953.96 eV (main) and 962.35 eV (satellite), and the Cu $2p_{3/2}$ main peak shifts slightly to 934.59 eV (Cu^{2+}) with satellite peaks at 944.01 eV and 941.38 eV. In Fig. 2e, the Fe 2p spectrum of CFO500 exhibits two Fe $2p_{3/2}$ main peaks at 711.27 eV (Fe^{3+}) and 709.81 eV (Fe^{2+}), along with a satellite peak at 718.82 eV. The Fe $2p_{1/2}$ region shows a main peak at 724.39 eV and a satellite peak at 731.54 eV. For CFO500-2%Ni, the Fe $2p_{3/2}$ peaks shift marginally to 711.37 eV (Fe^{3+}) and 709.91 eV (Fe^{2+}), with a satellite peak at 718.95 eV. The Fe $2p_{1/2}$ region shows a main peak at 724.48 eV and a satellite peak at 731.46 eV. Notably, the Fe^{3+}/Fe^{2+} peak area ratio decreases from 2.3 (CFO500) to 2.0 after 2% Ni doping (CFO500-2%Ni).

XPS was employed to characterize pure CuO and Fe_2O_3 samples as shown in Fig. S3, aiming to verify interfacial interactions and charge-transfer direction in Z-scheme systems. The Cu 2p spectra of CuO display a Cu $2p_{1/2}$ main peak at 952.77 eV and a satellite peak at 961.80 eV, along with Cu $2p_{3/2}$ peaks comprising a divalent-copper main peak at 933.46 eV with satellites at 941.05 eV and 943.46 eV, and a monovalent-copper peak at 932.44 eV, yielding a Cu^{2+}/Cu^{+} peak-area ratio of 2.3. In CFO500, the Cu^{2+} peak shifts to 933.95 eV, a 0.49 eV positive shift relative to CuO, with the Cu^{2+}/Cu^{+} ratio increasing to 4.9, indicating elevated high-valence copper and reduced low-valence copper. The Fe 2p spectra of Fe_2O_3 exhibit Fe $2p_{3/2}$ main peaks at 710.95 eV for Fe^{3+} and 709.62 eV for Fe^{2+} plus a satellite at 718.74 eV, and a Fe $2p_{1/2}$ main peak at 724.25 eV with a satellite at 730.96 eV, giving a Fe^{3+}/Fe^{2+} ratio of 3.5. For CFO500, the Fe^{3+} peak shifts to 711.27 eV, a 0.32 eV positive shift *versus* Fe_2O_3, while the Fe^{3+}/Fe^{2+} ratio decreases to 2.3, demonstrating increased low-valence iron and decreased high-valence iron. These spectral changes confirm electron transfer from CuO to Fe_2O_3, resulting in more Cu^{2+} and less Fe^{3+}.

Fig. 2f compares the O 1s spectra: for CFO500, peaks at 531.5 eV and 529.69 eV are attributed to surface chemisorbed oxygen and lattice oxygen, respectively. In CFO500-2%Ni, these peaks shift slightly to 531.60 eV (chemisorbed oxygen) and 529.77 eV (lattice oxygen). As shown in Table S2, the oxygen vacancy contribution (fitted from O 1s spectra) increases from 23% in CFO500 to 35% in CFO500-2%Ni. This indicates that Ni doping enhances oxygen vacancies on the surface, which can act as active sites to trap photogenerated electrons and suppress charge recombination.[27] As revealed by XPS depth profiling of CFO500-2%Ni (Fig. S4), nickel is uniformly distributed both inside and on the surface of the sample.

Fig. 3a shows the *I–t* curves obtained under a 500 W xenon lamp alternating between on and off. As the nickel doping ratio increases, the photocurrent response first decreases and then increases. Among the materials with different doping ratios, the enhanced photocurrent of CFO500-2%Ni (0.52 μA cm^{-2}) is attributed to Ni-induced surface states that facilitate electron trapping and suppress recombination, followed by CFO500-4%Ni (~0.5 μA cm^{-2}), then CFO500 (~0.29 μA cm^{-2}), and CFO500-1%Ni (~0.18 μA cm^{-2}) has the worst response. These curves also indicate that nickel doping can enhance

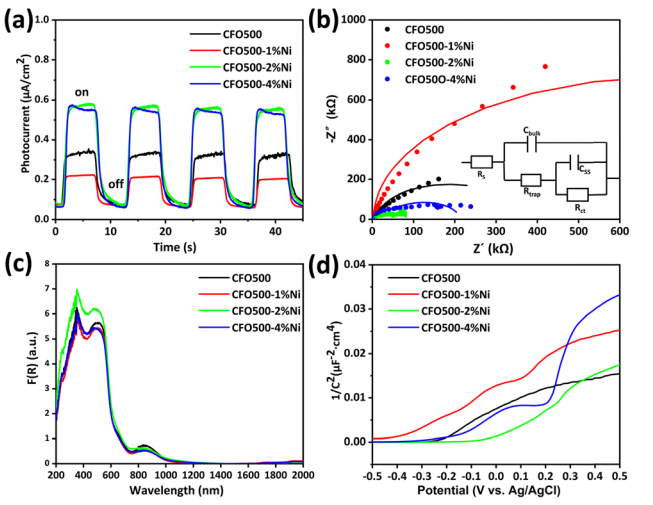

Fig. 3 (a) *I–t* curves; (b) EIS Nyquist plots under illumination; (c) transformed Kubelka–Munk reflectance spectra of CFO materials; (d) Mott–Schottky plots of CFO500, CFO500-1%Ni, CFO500-2%Ni and CFO500-4%Ni.

 This journal is © the Owner Societies 2025

Published on 01 septembrie 2025. Downloaded on 02.02.2026 22:20:06.

the response signal and improve the electron–hole separation efficiency of CFO500. In addition, after 4 ON/OFF light illumination cycles, the *I*–*t* curves of the four photocatalysts remain consistent, indicating that they have good photoelectric stability. Additionally, electrochemical impedance spectroscopy (EIS) was employed to investigate the charge transfer behavior at the interface between the photoelectrode and electrolyte (Fig. 3b). Fig. 3b shows the impedance of the materials fitted with an equivalent circuit, and the detailed fitting data are summarized in Table S3. The equivalent circuit consists of two parts: one represents the capture process of photogenerated electrons on the material surface (R_{trap} and C_{bulk}), and the other represents the transfer process of photogenerated electrons from the trapped states to the solution (R_{ct} and C_{ss}), where C_{ss} and R_{ct} denote the surface-state capacitance and charge transfer resistance, respectively.[28] Under light illumination, a higher C_{ss} value indicates more efficient trapping of photogenerated carriers, thereby suppressing their recombination; a lower R_{ct} value corresponds to a smaller impedance semicircle radius, which is favorable for charge transfer. The C_{ss} value of CFO500 was 5.39×10^{-6} F, and it gradually increased with the increase in nickel doping ratio. The CFO500-2%Ni sample exhibited a significantly enhanced C_{ss} value of 3.88×10^{-5} F, demonstrating greatly improved capability for trapping photogenerated carriers. Moreover, CFO500-2%Ni showed the smallest R_{ct} value of 5.25×10^{4} Ω, indicating the fastest charge transfer kinetics. These results suggest that 2% nickel doping exhibits the best optical response, which promotes photocatalytic hydrogen production.

Fig. 3c presents the Kubelka–Munk-transformed diffuse reflectance spectra of the as-prepared samples. The light absorption range of CFO includes ultraviolet light and part of the visible light range. Through Tauc equation calculations, we obtained the bandgap (E_g) of CFO500-2%Ni as 0.88 eV (as shown in Fig. S5). The positive slope of the Mott–Schottky plots in Fig. 3d indicates that CFO before and after doping are n-type semiconductors.

Surface photovoltage (SPV) spectroscopy and transient surface photovoltage (TPV) were employed to investigate the charge transfer behavior in CFO catalysts. Both techniques reveal polarity-dependent responses: positive signals indicate surface hole accumulation, while negative signals reflect electron migration to the surface. The amplitude of these signals demonstrates a direct linear relationship with charge separation efficiency. Notably, the SPV signal amplitude serves as a direct metric for evaluating electron–hole pair separation efficiency, where stronger signals correlate with enhanced charge dissociation.[29–32] Under 300–800 nm monochromatic illumination, the undoped sample displays a positive SPV signal as shown in Fig. 4a. Ni doping induces a gradual polarity inversion from positive to negative, demonstrating redirected electron transfer from the bulk to the surface. This confirms Ni-derived surface states act as electron traps, creating localized electron-rich zones that suppress recombination and enhance charge separation. CFO500-2%Ni exhibits the most pronounced negative SPV response, corresponding to optimal charge separation/transfer efficiency. The SPV spectra of Fe_2O_3 and CuO are shown in Fig. S6a and b. As shown in Fig. 4b, TPV spectra under 355 nm excitation reveal synchronized polarity inversion with increasing Ni content, where 2% Ni doping generates the strongest negative signal, which is consistent with SPV trends. CFO500-2%Ni exhibits delayed peak response times *versus* lower-doped counterparts, suggesting prolonged carrier lifetimes. Intermediate 1% Ni doping exhibits time-dependent signal inversion from positive to negative, reflecting progressive electron trapping by surface states. Exponential decay analysis (Table S4) confirms enhanced carrier lifetimes in CFO500-2%Ni (4.72 ms) *versus* undoped CFO500 (0.9 ms), aligning with its superior separation efficiency. It also resolves the electron capture process occurring in the sub millisecond time scale, with carrier lifetimes prolonged to 4.72 ms with a 5-fold enhancement. The dynamic process of capturing electrons by surface states requires a relatively long time, which can be observed by modulating the frequency of the photovoltaic voltage, as shown in Fig. 4c. When the testing frequency of the photovoltaic voltage is reduced, the duration of a single illumination cycle becomes longer, and the behavior of the photogenerated charge over a longer time scale is captured. Therefore, the photovoltaic response is negative, indicating that photogenerated electrons are enriched on the material surface by surface states for a long time. From Fig. S6c and d, it can be seen that for the CFO500 sample, its surface photovoltage response is positive, indicating that the migration of photogenerated holes to the surface dominates. For the CFO500-2%Ni sample, its surface photovoltage response is

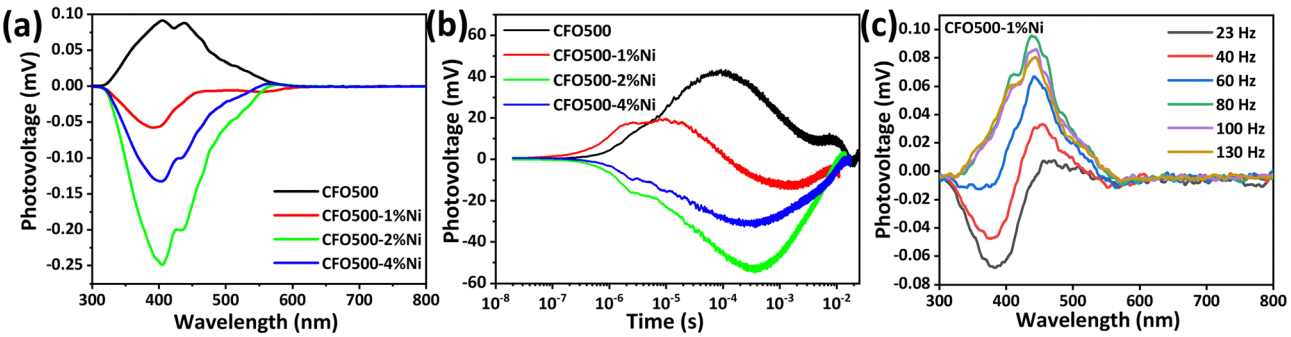

Fig. 4 (a) SPV spectra of CFO; (b) TPV spectra of CFO; (c) SPV frequency spectra of CFO.

Published on 01 septembrie 2025. Downloaded on 02.02.2026 22:20:06.

negative, indicating that the migration of photogenerated electrons to the surface dominates. No other processes were directly observed for either sample. From Fig. S7, it can be clearly seen that the electrochemical surface area of CFO500-2% Ni is significantly higher than that of CFO500, indicating that doping Ni can improve ECSA, which is beneficial for enhancing the ability of surface states to capture charges.

In order to evaluate the catalytic activity, we conducted photocatalytic hydrogen production experiments under simulated solar light conditions. As shown in Fig. 5a, the sample exhibited a substantial enhancement in catalytic performance under 10 W ultraviolet irradiation (355 nm). Control experiments revealed that the CFO500-2%Ni composite demonstrated optimal catalytic yield, achieving 1933.69 μmol g^{-1} h^{-1}. Fig. 5b illustrates the photochemical evaluation conducted under a full-spectrum irradiation system employing a 10 W LED lamp. The nickel-doped CFO500 catalyst maintained a maximum catalytic yield of 104.63 μmol g^{-1} h^{-1}. This is consistent with the previous SPV results showing that the surface of the CFO500-2%Ni material is enriched with the most photogenerated electrons. The photocatalytic performance of the material under UV light surpasses that under visible light. Firstly, this is because of the very weak absorption in the visible region, especially at wavelengths longer than 600 nm. Secondly, frequency-modulated photovoltage spectra reveal that under visible light, photogenerated holes migrate towards the material surface, as this migration is detrimental to photocatalytic hydrogen production. Finally, in the UV region, the surface photovoltage response is negative, indicating that photogenerated electrons migrate to the material surface, as this migration is beneficial for photocatalytic hydrogen production. The hydrogen production rates of Fe_2O_3 and CuO under a 10 W LED light are shown in Fig. S8. After four tests, the CFO500-2%Ni sample still maintained a hydrogen production rate close to its original rate without a significant decrease as shown in Fig. S9a and b, indicating favorable hydrogen production stability. SEM and XRD measurements were carried out for the sample after photocatalysis as shown in Fig. S9c and d. The retention of morphology along with XRD characteristic peaks maintaining their positions and relative ratios after stability testing confirms the good stability of CFO during long-term photocatalysis. After the photocatalytic reaction, the gas chromatogram of the products is shown in Fig. S10. It can be seen that no other by-products were detected besides the hydrogen product. The nitrogen peak in the chromatogram originates from the nitrogen gas introduced during the photocatalytic process. Comparison of photocatalytic hydrogen evolution reaction performance over various photocatalysts and reaction conditions reported in the literature is summarized in Table S5.

Mott–Schottky plots, Tauc plots, and density functional theory (DFT) calculations were conducted on CuO and Fe_2O_3 to determine their band edge potentials and work functions, as shown in Fig. S11, supporting the charge transfer mechanism. Mott–Schottky plots for CuO and Fe_2O_3 measured at 1000 Hz are shown in Fig. S11a and b; the positive slope indicates that Fe_2O_3 is an n-type semiconductor, whereas the negative slope confirms CuO as a p-type semiconductor. The flat-band potential, determined from the tangent intercept of the Mott–Schottky plots on the *X*-axis, is 0.66 V *vs.* Ag/AgCl for CuO (reasonably approximating its valence band) and −0.26 V *vs.* Ag/AgCl for Fe_2O_3 (reasonably approximating its conduction band). Fig. S11c and d show the Tauc plots derived from the UV-vis DRS spectra of CuO and Fe_2O_3, revealing band-gap values of 1.23 eV for CuO and 2.29 eV for Fe_2O_3. The conduction band of CuO is thus calculated at −0.57 V *vs.* Ag/AgCl, and the valence-band (VB) potential of Fe_2O_3 at 2.03 V *vs.* Ag/AgCl. Considering the relative VB edge positions, CuO and Fe_2O_3 form a Z-scheme heterojunction. Work function calculations further confirm charge transfer between CuO and Fe_2O_3 as shown in Fig. S11e and f. With a work function of 5.445 eV for Fe_2O_3 exceeding that of CuO (4.722 eV), the Fermi level of Fe_2O_3 is lower than CuO. Upon contact, charge transfer occurs with electrons moving from CuO to Fe_2O_3, forming a built-in electric field directed from CuO to Fe_2O_3. Consequently, under illumination, photogenerated electrons transfer from Fe_2O_3 to CuO. The above evidence supports the Z-scheme charge transfer mechanism. Fig. 6 presents the charge transport mechanism in Ni-doped Fe_2O_3/CuO heterojunctions for photocatalytic hydrogen production. The introduction of nickel atoms selectively generates specific surface states on CuO, creating efficient photogenerated electron trapping sites. This effect originates from the effective establishment of a Z-scheme charge transfer mechanism within the heterojunction: the preferential annihilation of photogenerated holes in CuO with photogenerated electrons in Fe_2O_3 through interfacial

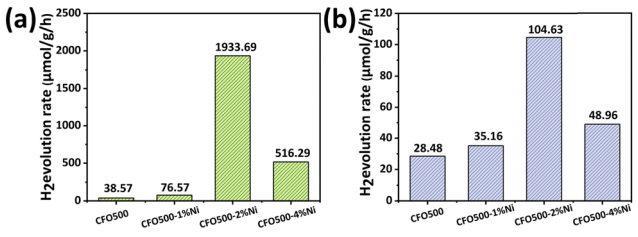

Fig. 5 (a) The catalytic activity of gas products of different samples under the illumination of a 10 W ultraviolet light with a wavelength of 355 nm; (b) the catalytic activity of gas products of different samples under the illumination of a 10 W LED light.

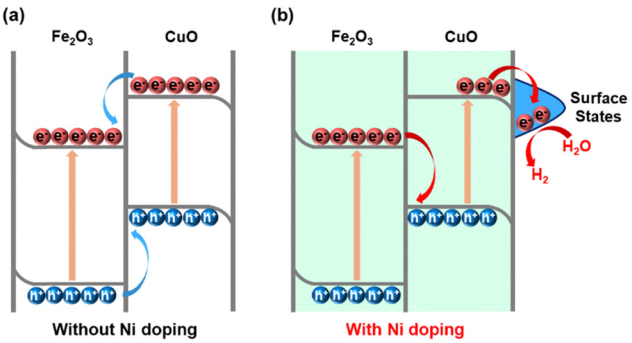

Fig. 6 Diagram of the photocatalytic water cracking mechanism of photocatalysts for CFO500 (a) and CFO500-2%Ni (b).

 This journal is © the Owner Societies 2025

Published on 01 septembrie 2025. Downloaded on 02.02.2026 22:20:06.

recombination channels effectively blocks the carrier recombination pathway mediated by Ni-induced surface states. Density of states analysis (Fig. S12) reveals that nickel doping induces surface state energy levels precisely localized near the conduction band minimum (CBM) of CuO, forming directionally aligned trapping centers that are energetically matched with photogenerated electrons. Notably, the 2% nickel doping concentration triggers a functional transformation of surface states and their fundamental nature evolves from simple charge trapping sites to dynamic electron storage media. This transformation optimizes both the spatial distribution of carriers and their transport kinetics, ultimately leading to significant enhancement of the hydrogen evolution performance in the heterojunction system. In the absence of Ni-doping, the Z-scheme charge-transfer engineering merely enables recombination of Fe_2O_3 conduction-band electrons with CuO valence-band holes to annihilate the latter, yet the surface states themselves can still act as recombination centers. This results in only limited charge accumulation at the surface and consequently weak hydrogen-evolution activity. Upon doping with 2 at% Ni, the Ni-mediated surface states are converted into electron reservoirs, achieving a synergistic extension of carrier lifetime and utilization efficiency, and thus markedly enhanced hydrogen-evolution capability.

Conclusion

In summary, the charge separation function of Ni-mediated surface states is reactivated *via* Z-scheme charge transfer engineering in Fe_2O_3/CuO heterojunctions, where photogenerated holes in CuO are driven to the interface and recombine with photogenerated electrons in Fe_2O_3, effectively blocking the carrier recombination pathway mediated by surface states. The photocatalyst exhibits excellent catalytic activity, which can be attributed to Ni doping in the Fe_2O_3/CuO heterojunction inducing the spontaneous accumulation of photo-induced electrons in the surface states, forming an electron reservoir that achieves a synergistic enhancement of carrier lifetime and utilization efficiency. Specifically, the sample doped with 2% Ni achieved a hydrogen evolution rate of 1933.69 μmol g^{-1} h^{-1}, which is approximately 50 times that of the original sample. This work not only elucidates the mechanism of transition metal dopants in regulating surface states but also provides a new paradigm for designing photocatalytic interfaces with dynamic electron accumulation capabilities.

Author contributions

Tengfei Jiang conceived and designed the experiments, Ke Ma analyzed the data and wrote the paper, Jingying Wei performed the experiments and analyzed the data, Dongfen Hou performed the experiments and collected the data, Dailing Jia performed the experiments and collected the data, Chun Guo performed the experiments and revised the manuscript, Huaiguo Xue designed the project and revised the manuscript, and Jingqi Tian conceived and designed the experiments, and revised the manuscript.

Conflicts of interest

The authors declare no competing financial interests.

Data availability

The data supporting this article have been included as part of the SI. Supplementary information available: Elemental distribution mapping, HRTEM and EDS spectra, XRD Rietveld analysis, XPS spectra, Tauc diagrams, SPV spectra, ECSA measurements, catalytic activity, DOS, fitting results of Nyquist plots, charge lifetime, and comparison of photocatalytic HER performances. See DOI: **https://doi.org/10.1039/d5cp02648b**

Acknowledgements

This research is financially supported by the National Natural Science Foundation of China (grant no. 22102140), the Natural Science Foundation of Jiangsu Province (grant no. BK20211602), the Specially Appointed Professor Plan in Jiangsu Province, and the Qing Lan Project of Yangzhou University.

Notes and references

1 A. Soto-Arreola, A. M. Huerta-Flores, J. M. Mora-Hernández and L. M. Torres-Martínez, Comparative study of the photocatalytic activity for hydrogen evolution of MFe_2O_4 (M = Cu, Ni) prepared by three different methods, *J. Photochem. Photobiol., A*, 2018, **357**, 20–29.

2 J. L. Domínguez-Arvizu, *et al.*, Optical properties determination of $NiFe_2O_4$ nanoparticles and their photocatalytic evaluation towards hydrogen production, *Int. J. Hydrogen Energy*, 2017, **42**, 30242–30248.

3 Z. Dedong, *et al.*, TiO_2@$ZnFe_2O_4$ heterojunctions for effecicent photocatalytic degradation of persistent pollutants and hydrogen evolution, *Mater. Chem. Phys.*, 2021, **277**, 125462.

4 B. Xia, *et al.*, TiO_2/$FePS_3$ S-Scheme Heterojunction for Greatly Raised Photocatalytic Hydrogen Evolution, *Adv. Energy Mater.*, 2022, **12**, 2201449.

5 F. Dai, *et al.*, Pt-surface oxygen vacancies coupling accelerated photo-charge extraction and activated hydrogen evolution, *Nano Res.*, 2023, **16**, 4736–4741.

6 T. Li, L. Zhang, X. Li, X. Wang and Z. Jin, Design and synthesis of phosphating bimetallic CeCo-MOF for substantially improved photocatalytic hydrogen evolution, *J. Mater. Chem. C*, 2022, **10**, 8750–8761.

7 I. Ahmad, *et al.*, Recent progress in ZnO-based heterostructured photocatalysts: A review, *Mater. Sci. Semicond. Process.*, 2024, **180**, 108578.

8 I. Ahmad, *et al.*, Improved hydrogen production performance of an S-scheme Nb_2O_5/La_2O_3 photocatalyst, *Dalton Trans.*, 2025, **54**, 1402–1417.

9 M. Yuan, *et al.*, 0D/2D Ti^{3+}-TiO_2/P-doped g-C_3N_4 S-scheme heterojunctions for efficient photocatalytic H2 evolution, *Mater. Sci. Semicond. Process.*, 2024, **184**, 108858.

Published on 01 septembrie 2025. Downloaded on 02.02.2026 22:20:06.

10 X. Wang, *et al.*, High-energy ball-milling constructing P-doped g-C_3N_4/MoP heterojunction with MoN bond bridged interface and Schottky barrier for enhanced photocatalytic H2 evolution, *Appl. Catal., B*, 2022, **303**, 120933.
11 X. Li, *et al.*, Mott–Schottky Effect Leads to Alkyne Semihydrogenation over Pd-Nanocube@N-Doped Carbon, *ACS Catal.*, 2019, **9**, 4632–4641.
12 I. Ahmad, *et al.*, Boosted hydrogen evolution activity from Sr doped ZnO/CNTs nanocomposite as visible light driven photocatalyst, *Int. J. Hydrogen Energy*, 2021, **46**, 26711–26724.
13 H. Zhu, *et al.*, Surface states as electron transfer pathway enhanced charge separation in TiO2 nanotube water splitting photoanodes, *Appl. Catal., B*, 2018, **234**, 100–108.
14 B. K. Jha, S. Chaule and J.-H. Jang, Enhancing photocatalytic efficiency with hematite photoanodes: principles, properties, and strategies for surface, bulk, and interface charge transfer improvement, *Mater. Chem. Front.*, 2024, **8**, 2197–2226.
15 C. Ye, D.-S. Zhang, B. Chen, C.-H. Tung and L.-Z. Wu, Interfacial Charge Transfer Regulates Photoredox Catalysis, *ACS Cent. Sci.*, 2024, **10**, 529–542.
16 Q. Wu, *et al.*, Surface Electron Localization in Cu-MOF-Bonded Double-Heterojunction Cu_2O Induces Highly Efficient Photocatalytic CO2 Reduction, *ACS Appl. Mater. Interfaces*, 2022, **14**, 54328–54337.
17 Z. Zhang, *et al.*, Interfacial oxygen vacancies yielding long-lived holes in hematite mesocrystal-based photoanodes, *Nat. Commun.*, 2019, **10**, 4832.
18 A. V. Akimov, A. J. Neukirch and O. V. Prezhdo, Theoretical Insights into Photoinduced Charge Transfer and Catalysis at Oxide Interfaces, *Chem. Rev.*, 2013, **113**, 4496–4565.
19 X. Zhou and H. Dong, A Theoretical Perspective on Charge Separation and Transfer in Metal Oxide Photocatalysts for Water Splitting, *ChemCatChem*, 2019, **11**, 3688–3715.
20 P. Cui and Y. Xue, Sulfication-induced non-radiative electron-hole recombination dynamics in graphene quantum dots for tuning photocatalytic performance, *Spectrochim. Acta, Part A*, 2023, **287**, 122117.
21 K. Sivula, Metal Oxide Photoelectrodes for Solar Fuel Production, Surface Traps, and Catalysis, *J. Phys. Chem. Lett.*, 2013, **4**, 1624–1633.
22 L. Zhang, *et al.*, Effects of different defective linkers on the photocatalytic properties of Cu-BTC for overall water decomposition, *Appl. Catal., B*, 2022, **303**, 120888.
23 J. Ma, R. Long, D. Liu, J. Low and Y. Xiong, Defect Engineering in Photocatalytic Methane Conversion, *Small Structures*, 2022, **3**, 2100147.
24 I. Ahmad, S. Shukrullah, M. Y. Naz and H. N. Bhatti, A Cu medium designed Z-scheme ZnO–Cu–CdS heterojunction photocatalyst for stable and excellent H2 evolution, methylene blue degradation, and CO2 reduction, *Dalton Trans.*, 2023, **52**, 6343–6359.
25 I. Ahmad, S. Shukrullah, M. Y. Naz and H. N. Bhatti, Dual S-scheme ZnO–g-C_3N_4–CuO heterosystem: a potential photocatalyst for H2 evolution and wastewater treatment, *React. Chem. Eng.*, 2023, **8**, 1159–1175.
26 I. Ahmad, *et al.*, Strategies for optimizing sunlight conversion in semiconductor photocatalysts: A review of experimental and theoretical insights, *Int. J. Hydrogen Energy*, 2024, **96**, 1006–1066.
27 W. Zhou and H. Fu, Defect-mediated electron–hole separation in semiconductor photocatalysis, *Inorg. Chem. Front.*, 2018, **5**, 1240–1254.
28 L. Luo, *et al.*, A new and highly efficient co-catalyst Zn-Ni_5P_4 for photocatalytic H2 evolution with the reduced capacitance via Zn doping, *Appl. Catal., B*, 2023, **321**, 122008.
29 B. Wang, *et al.*, Direct evidence of Z-scheme effect and charge transfer mechanism in titanium oxide and cadmium sulfide heterostructure, *Colloids Surf., A*, 2021, **626**, 127086.
30 Y. Li, *et al.*, An effective CdS/Ti-Fe_2O_3 heterojunction photoanode: Analyzing Z-scheme charge-transfer mechanism for enhanced photoelectrochemical water-oxidation activity, *Chin. J. Catal.*, 2021, **42**, 762–771.
31 I. Levine, *et al.*, Charge transfer rates and electron trapping at buried interfaces of perovskite solar cells, *Joule*, 2021, **5**, 2915–2933.
32 F. Wu, K. Zhan, T. Zhang, R. Jian and Q. Qiao, Exploring charge behavior at the terminal surface and charge separation interface of organo-lead perovskite using in situ surface photovoltage spectroscopy, *Phys. Chem. Chem. Phys.*, 2023, **25**, 11075–11079.

 This journal is © the Owner Societies 2025